6

Synthesis: Viscous, Diffusive, Inhomogeneous, Parallel Shear Flow

In this chapter we explore equilibria and perturbations in a stratified, parallel shear flow with the effects of viscosity and diffusion included, effectively unifying Chapters 2, 3, 4, and 5. The goal is to develop numerical solution methods that have wide applicability to the study of small-scale processes in the oceans and atmosphere and explore some applications of those methods.

6.1 Expanding the Basic Equations

We start with the Boussinesq equations for a viscous, diffusive, inhomogeneous fluid. The divergence equation is, as usual,

$$\vec{\nabla} \cdot \vec{u} = 0.$$

The momentum equation (1.19), neglecting the Coriolis acceleration but retaining viscosity and restoring buoyancy, is

$$\frac{D\vec{u}}{Dt} = -\vec{\nabla}\pi + b\hat{e}^{(z)} + \nu\nabla^2\vec{u}, \tag{6.1}$$

and the buoyancy equation (1.25) is

$$\frac{Db}{Dt} = \kappa\nabla^2 b. \tag{6.2}$$

We assume the perturbation solution

$$\vec{u} = U(z,t)\hat{e}^{(x)} + \epsilon\vec{u}',$$
$$b = B(z,t) + \epsilon b',$$
$$\pi = \Pi + \epsilon\pi'. \tag{6.3}$$

At this stage, we have not yet assumed that the background state (U, B, Π) is steady. No assumption is made regarding the background pressure Π.

153

6.1.1 Continuity

As usual we deal with the easiest equation first:

$$\vec{\nabla} \cdot \vec{u}' = 0.$$

6.1.2 Momentum

The momentum equation (6.1), with the perturbation solution (6.3), becomes

$$\left[\frac{\partial}{\partial t} + U \frac{\partial}{\partial x} + \varepsilon \vec{u}' \cdot \vec{\nabla} \right] \left[U(z, t) \hat{e}^{(x)} + \varepsilon \vec{u}' \right]$$
$$= -\vec{\nabla} \left(\Pi + \varepsilon \pi' \right) + \left(B(z, t) + \varepsilon b' \right) \hat{e}^{(z)} + \nu \nabla^2 \left[U(z, t) \hat{e}^{(x)} + \varepsilon \vec{u}' \right]. \quad (6.4)$$

With $\epsilon = 0$, this gives the three component equations:

$$\frac{\partial U}{\partial t} = -\frac{\partial \Pi}{\partial x} + \nu \frac{\partial^2 U}{\partial z^2} \quad (6.5)$$

$$0 = -\frac{\partial \Pi}{\partial y} \quad (6.6)$$

$$0 = -\frac{\partial \Pi}{\partial z} + B. \quad (6.7)$$

The first equation shows that the background flow is governed by the combination of the streamwise pressure gradient and viscosity, as we saw previously in section 5.1. Strict equilibrium ($\partial U/\partial t = 0$) can be satisfied only when $\partial^2 U/\partial z^2 = $ const.[1] As in the homogeneous case, the "frozen flow" approximation holds provided $\sigma^\star \gg 1/Re$ (section 5.2). The second equation shows that the background pressure does not depend on y, while the third describes hydrostatic balance between the vertical pressure gradient and the buoyancy.

At $O(\epsilon)$, (6.4) gives

$$\left(\frac{\partial}{\partial t} + U \frac{\partial}{\partial x} \right) \vec{u}' + U_z w' \hat{e}^{(x)} = -\vec{\nabla} \pi' + b' \hat{e}^{(z)} + \nu \nabla^2 \vec{u}'. \quad (6.8)$$

Observe that this perturbation momentum equation combines the terms seen previously in (2.14), (3.7), (4.7), and (5.13).

6.1.3 Buoyancy

Substitution of (6.3) into (6.2) gives

$$\left[\frac{\partial}{\partial t} + U \frac{\partial}{\partial x} + \varepsilon \vec{u}' \cdot \vec{\nabla} \right] \left[B(z, t) + \varepsilon b' \right] = \kappa \nabla^2 \left[B(z, t) + \varepsilon b' \right]. \quad (6.9)$$

---

[1] Set $\partial U/\partial t = 0$ in (6.5) then cross-differentiate with (6.7) to eliminate Π. You'll find that $\partial^3 U/\partial z^3 = 0$.

For the unperturbed flow, this is

$$\frac{\partial B}{\partial t} = \kappa \frac{\partial^2 B}{\partial z^2} \tag{6.10}$$

Strict equilibrium requires that both sides vanish, hence

$$\frac{\partial B}{\partial z} = N^2 = \text{const.},$$

as was seen in section 2.7.

Repeating the arguments we used in the previous chapter for inhomogeneous flows, we can show that quasi-equilibrium requires

$$\sigma^\star \gg \frac{1}{Re\,Pr},$$

where $\sigma^\star = \sigma h/u_0$ is the growth rate scaled by the background shear, Re is the Reynolds number, and $Pr = \nu/\kappa$ is the Prandtl number. If $Pr \geq 1$, then the previous condition $\sigma^\star \gg 1/Re$ is sufficient.

The perturbation part of (6.9) is obtained by subtracting (6.10) and omitting terms of order ϵ^2:

$$\left(\frac{\partial}{\partial t} + U\frac{\partial}{\partial x}\right)b' + B_z w' = \kappa \nabla^2 b'. \tag{6.11}$$

Note that (6.11) combines the buoyancy perturbation equations for a motionless, inhomogeneous fluid (2.12), and a stratified, nondiffusive, parallel shear flow (4.10).

6.1.4 Eliminating the Pressure

We eliminate the pressure, as we have done before, by combining the divergence of (6.8) with the Laplacian of its vertical component. The divergence gives the pressure equation:[2]

$$\nabla^2 \pi' = -2U_z \frac{\partial w'}{\partial x} + \frac{\partial b'}{\partial z}. \tag{6.12}$$

Taking the Laplacian of the vertical component of (6.8) and substituting the vertical derivative of (6.12), we obtain:

$$\left(\frac{\partial}{\partial t} + U\frac{\partial}{\partial x}\right)\nabla^2 w' - U_{zz}\frac{\partial w'}{\partial x} = \nabla_H^2 b' + \nu \nabla^4 w'. \tag{6.13}$$

In (6.13) and (6.11), we have two equations for the two unknowns w' and b'. It is possible to combine these further into a single equation, but we will not do that

---

[2] Compare this with equations (2.16) and (3.11).

here. Instead, we substitute the normal mode forms $w' = \{\hat{w}(z)e^{\sigma t}e^{\iota(kx+\ell y)}\}_r$ and $b' = \{\hat{b}(z)e^{\sigma t}e^{\iota(kx+\ell y)}\}_r$ to obtain a pair of ordinary differential equations:

$$\boxed{(\sigma + \iota kU)\nabla^2\hat{w} - \iota kU_{zz}\hat{w} = -\tilde{k}^2\hat{b} + \nu\nabla^4\hat{w}} \tag{6.14}$$

$$\boxed{(\sigma + \iota kU)\hat{b} + B_z\hat{w} = \kappa\nabla^2\hat{b},} \tag{6.15}$$

where $\nabla^2 = d^2/dz^2 - \tilde{k}^2$.

6.2 Numerical Solution

Viscous and diffusive effects complicate the stability analysis, and in many problems they are not of central interest. Even so, the added effort is well justified. Computing instabilities of inviscid stratified shear flows requires extremely fine grid resolution, and can therefore be very slow. The inclusion of very weak viscosity, e.g., $Re = 10^6$, stabilizes the numerical algorithm and thereby approximates the inviscid result with much lower computational cost.

The normal mode equations (6.14) and (6.15) can be written in matrix form:

$$\sigma \begin{pmatrix} \nabla^2 & 0 \\ 0 & 1 \end{pmatrix} \begin{pmatrix} \hat{w} \\ \hat{b} \end{pmatrix} = \begin{pmatrix} -\iota kU\nabla^2 + \iota kU_{zz} + \nu\nabla^4 & -\tilde{k}^2 \\ -B_z & -\iota kU + \kappa\nabla^2 \end{pmatrix} \begin{pmatrix} \hat{w} \\ \hat{b} \end{pmatrix}.$$

These are discretized to form a generalized eigenvalue problem with $2N \times 2N$ matrices:

$$\sigma \, \mathsf{A}\vec{x} = \mathsf{B}\vec{x}.$$

The eigenvector $\vec{x}$ is a concatenation of the discretized forms of $\hat{w}$ and $\hat{b}$:

$$\vec{x} = \begin{pmatrix} \hat{w}_1 \\ \hat{w}_2 \\ \vdots \\ \hat{w}_N \\ \hat{b}_1 \\ \hat{b}_2 \\ \vdots \\ \hat{b}_N \end{pmatrix},$$

and the matrices are

$$\mathsf{A} = \begin{pmatrix} \nabla^2 & 0 \\ 0 & \mathsf{I} \end{pmatrix}$$

$$\mathsf{B} = \begin{pmatrix} -\iota k\vec{U} \cdot \nabla^2 + \iota k\vec{U}_{zz} \cdot \mathsf{I} + \nu\nabla^4 & -\tilde{k}^2\mathsf{I} \\ -\vec{B}_z \cdot \mathsf{I} & -\iota k\vec{U} \cdot \mathsf{I} + \kappa\nabla^2 \end{pmatrix}.$$

Each matrix is composed of four $N \times N$ submatrices, which in turn are combinations of the Laplacian, the squared Laplacian, and input vectors U and B defined in the usual way. Left-multiplications such as $\vec{U} \cdot \nabla^2$ are computed as described in section 3.5.2.

6.2.1 Boundary Conditions

As in the homogeneous case, we assume that $\hat{w} = 0$ at the boundaries. We also have the choice of rigid ($\hat{w}_z = 0$) or frictionless ($\hat{w}_{zz} = 0$) boundaries.

For an inhomogeneous fluid, we also need boundary conditions for the buoyancy, and again there are two choices. First, we can assume that the buoyancy at the boundary is fixed, i.e., the perturbation from equilibrium is zero:

$$\hat{b} = 0.$$

The second choice is that the boundary is insulating, i.e., the diffusive buoyancy flux $-\kappa \, \partial b / \partial z$ vanishes. In normal mode form, this is expressed as

$$\hat{b}_z = 0.$$

Insulating boundaries, like frictionless boundaries, are often preferable in cases where there is no physical boundary, because they have minimal effect.

For the numerical solution described above, we need a matrix to compute the second-derivative of $\hat{b}$, and that matrix must incorporate the appropriate boundary conditions. In the case of fixed-buoyancy boundaries, the matrix can be exactly the same as we use to compute the second-derivative of $\hat{w}$, because the boundary condition is mathematically identical to $\hat{w} = 0$. But in the case of insulating boundaries, a separate second-derivative matrix is needed. The design of that matrix is the same as that described in section 5.5.

6.2.2 A Note on Applications

The theory encompassed in (6.14) and (6.15) includes every case we have discussed in Chapters 2, 3, 4, and 5 as special cases. For example, we can look at solutions of the Orr-Sommerfeld equation for homogeneous, viscous flows by setting $B_z = 0$. We can solve the Benard problem (section 2.4) by setting $U = 0$ and B_z to a negative constant. We can also combine these problems, e.g., to find the effect of stratification on the Tollmein-Schlichting instability, or the effect of shear on Benard convection (problem 19).

Solutions of the Taylor-Goldstein equation for inviscid stratified shear flows (Chapter 4) are obtained by setting $\nu = \kappa = 0$. These include all of the wavelike phenomena listed in section 4.5: internal gravity waves, vortical waves, baroclinic normal modes as well as the vertical structure functions used in the description of

internal solitary waves, bores, and hydraulic jumps. In practice, one sets ν and κ to small but nonzero values. This gives close approximations to the inviscid limit but minimizes distortions due to roundoff error, and is therefore the preferred method for solving the Taylor-Goldstein equation.

The above methods lead to a solution procedure $\mathcal{F}$ for the analysis of viscous, diffusive, stratified, parallel shear flows. It is most commonly a subroutine. Having written and tested the subroutine, we treat it as a "black box," which accepts inputs and gives back outputs but does not need to be modified internally. If used correctly, $\mathcal{F}$ can solve a vast range of problems, based both on idealized models and on observational data. In the following sections 6.3 and 6.4, we will discuss different ways of defining the inputs and interpreting the outputs so that $\mathcal{F}$ will be maximally useful.

6.3 2D and Oblique Modes: Squire Transformations

Here, we consider the effect of stratification, viscosity, and diffusion on the growth rates of oblique modes. Recall that an oblique mode is one whose wave vector (k, ℓ) points at a nonzero angle φ from the x axis, the angle of obliquity. The corresponding 2D mode has a wave vector of the same magnitude, $\tilde{k}$, but parallel to the x axis (Figure 3.10).

6.3.1 Transforming the Buoyancy

Consider an oblique mode that obeys the equations for viscous, diffusive, stratified shear flow:

$$(\sigma + \iota k U)\nabla^2 \hat{w} - \iota k U_{zz}\hat{w} = -\tilde{k}^2 \hat{b} + \nu \nabla^4 \hat{w} \qquad (3D1)$$

$$(\sigma + \iota k U)\hat{b} + B_z \hat{w} = \kappa \nabla^2 \hat{b}, \qquad (3D2)$$

where

$$\nabla^2 = \frac{d^2}{dz^2} - \tilde{k}^2 \; ; \quad \tilde{k} = \sqrt{k^2 + \ell^2}.$$

Suppose also that we have a solution algorithm

$$\sigma = \mathcal{F}(z, U, B_z, \nu, \kappa; \; k, \ell). \qquad (6.16)$$

The corresponding 2D mode with wave vector $(\tilde{k}, 0)$ obeys:

$$(\sigma + \iota \tilde{k} U)\nabla^2 \hat{w} - \iota \tilde{k} U_{zz}\hat{w} = -\tilde{k}^2 \hat{b} + \nu \nabla^4 \hat{w} \qquad (2D1)$$

$$(\sigma + \iota \tilde{k} U)\hat{b} + B_z \hat{w} = \kappa \nabla^2 \hat{b}, \qquad (2D2)$$

and therefore has the solution algorithm $\sigma_{2D} = \mathcal{F}(z, U, B_z, \nu, \kappa; \; \tilde{k}, 0)$.

Is there a transformation that makes these ($2D$) equations isomorphic with the ($3D$)? We begin by defining the Squire transformations

$$\sigma = \cos\varphi\,\tilde\sigma; \quad \hat b = \cos\varphi\,\tilde{\hat b}; \quad \nu = \cos\varphi\,\tilde\nu.$$

Now substitute these into ($3D1$) and divide out the common factor $\cos\varphi$. The result is isomorphic to ($2D1$).

$$(\tilde\sigma + \imath\tilde k U)\nabla^2\hat w - \imath\tilde k U_{zz}\hat w = -\tilde k^2\tilde{\hat b} + \tilde\nu\nabla^4\hat w. \tag{$\widetilde{3D1}$}$$

Turning to equations ($3D2$) and ($2D2$), we now define two more transformations:

$$B_z = \cos^2\varphi\,\tilde B_z; \quad \kappa = \cos\varphi\,\tilde\kappa.$$

Substituting into ($3D2$) and dividing out $\cos^2\varphi$, we obtain:

$$(\tilde\sigma + \imath\tilde k U)\tilde{\hat b} + \tilde B_z\hat w = \tilde\kappa\nabla^2\tilde{\hat b}. \tag{$\widetilde{3D2}$}$$

With all these transformations, ($\widetilde{3D1}$) and ($\widetilde{3D2}$) are isomorphic to ($2D1$) and ($2D2$), respectively, and can therefore be solved using the same solution algorithm: $\tilde\sigma = \mathcal{F}(z, U, \tilde B_z, \tilde\nu, \tilde\kappa;\ \tilde k, 0)$, or

$$\sigma_{3D} = \cos\varphi \times \mathcal{F}\left(z, U, \frac{B_z}{\cos^2\varphi}, \frac{\nu}{\cos\varphi}, \frac{\kappa}{\cos\varphi};\ \tilde k, 0\right).$$

The growth rate of the 3D mode is $\cos\varphi$ times that of a corresponding 2D mode that exists in a fluid with increased viscosity, diffusivity and stratification. In most circumstances this means that the oblique mode will have a slower growth rate, but if any of those three factors should increase the growth rate, and do so rapidly enough to compensate for the factor $\cos\varphi$, then the oblique mode can grow faster.

6.3.2 Oblique and Veering Flows: Transforming the Velocity

In the inviscid case we found that a normal mode perturbation in a shear flow is affected only by the component of the background flow that is parallel to its own wave vector (section 4.3, Figure 4.7). The same is true in a viscous fluid, as we now confirm. As before, we define the transformed background velocity profile

$$\tilde U(z) = \frac{k}{\tilde k}\,U(z) = \cos\varphi\,U(z). \tag{6.17}$$

Now, everywhere in ($3D1, 2$), replace kU with $\tilde k\tilde U$:

$$(\sigma + \imath\tilde k\tilde U)\nabla^2\hat w - \imath\tilde k\tilde U_{zz}\hat w = -\tilde k^2\hat b + \nu\nabla^4\hat w \tag{$\widetilde{3D1}$}$$

$$(\sigma + \imath\tilde k\tilde U)\hat b + B_z\hat w = \kappa\nabla^2\hat b. \tag{$\widetilde{3D2}$}$$

This set is isomorphic to $(2D1, 2)$ under the transformation (6.17), and therefore has the same solution algorithm:

$$\sigma_{3D} = \mathcal{F}(z, \tilde{U}, B_z, \nu, \kappa; \; \tilde{k}, 0). \tag{6.18}$$

For a typical shear instability, this means that the growth rate of the 3D mode will be reduced relative to the corresponding 2D mode. There are cases where this is not true, though. Recall the definitions of the Reynolds and bulk Richardson numbers:

$$Re = \frac{hu_0}{\nu} \; ; \quad Ri_b = \frac{b_0 h}{u_0^2},$$

A decrease in u_0 decreases Re and increases Ri_b, and if either of these changes should increase the growth rate, a 3D mode may be the most unstable (see the example below). Also, some instabilities, such as convection, turn out to be damped by shear, so that reducing u_0 increases the growth rate, with interesting results as you will see in homework project 19.

As in the inviscid case (section 4.12), the solution algorithm (6.18) for parallel flows is easily extended to handle veering flows by replacing (6.17) with the more general definition:

$$\boxed{\tilde{U}(z) = \frac{kU(z) + \ell V(z)}{\tilde{k}}.} \tag{6.19}$$

In practice, one loops over a range of wave vectors (k, ℓ) and repeats the stability analysis for each case using $\tilde{U}(z)$ as given by (6.19).

6.4 Shear and Diffusion Scalings

The normal mode equations for a viscous, diffusive, stratified, parallel shear flow are [reproducing (6.14) and (6.15)]

$$(\sigma + \iota kU)\nabla^2 \hat{w} - \iota k U_{zz} \hat{w} = -\tilde{k}^2 \hat{b} + \nu \nabla^4 \hat{w} \tag{6.20}$$

$$(\sigma + \iota kU)\hat{b} + B_z \hat{w} = \kappa \nabla^2 \hat{b}, \tag{6.21}$$

where $\nabla^2 = d^2/dz^2 - \tilde{k}^2$ as usual. Suppose that we have a solution algorithm

$$[\sigma, \hat{w}, \hat{b}] = \mathcal{F}(z, U, B_z, \nu, \kappa; \; k, \ell). \tag{6.22}$$

We now introduce a general length scale L and velocity scale V and use them to define nondimensional equivalents for the quantities in (6.20) and (6.22):

$$z^\star = \frac{z}{L}$$

$$U^\star = \frac{U}{V} \; ; \quad \hat{w}^\star = \frac{\hat{w}}{V}$$

$$\sigma^\star = \sigma \frac{L}{V}$$

$$\{k^\star, \ell^\star, \tilde{k}^\star\} = \{k, \ell, \tilde{k}\}L$$

$$\frac{d}{dz} = \frac{1}{L} \frac{d}{dz^\star} \quad \Rightarrow \nabla^2 = \frac{1}{L^2} \left(\frac{d^2}{dz^{\star 2}} - \tilde{k}^{\star 2} \right)$$

$$v^\star = \frac{v}{LV} \; ; \quad \kappa^\star = \frac{\kappa}{LV}$$

$$B^\star = B \frac{L}{V^2} \; ; \quad \hat{b}^\star = \hat{b} \frac{L}{V^2}. \tag{6.23}$$

By substitution, one may now write a scaled version of (6.20, 6.21) and show that it is isomorphic to the original version (the student should do this), so that the same solution algorithm holds:

$$[\sigma^\star, \hat{w}^\star, \hat{b}^\star] = \mathcal{F}(z^\star, U^\star, B^\star_{z^\star}, v^\star, \kappa^\star; \; k^\star, \ell^\star). \tag{6.24}$$

Choices for the scales L and V are endless. We will look at two particularly useful choices: shear scaling and diffusion scaling.

While these generalized scalings always "work," i.e., you can input them to the solution procedure and get the correct (scaled) answer as in (6.24), they are not necessarily the most natural scalings for a particular problem. For example, although V^2/L has the right units for a buoyancy scale, it has no logical connection to buoyancy. It may be more natural to define a separate buoyancy scale b_0, so that

$$B = b_0 \beta,$$

where β is a nondimensional function. As an example, perhaps the background buoyancy profile is $B = b_0 \tanh \frac{z}{L}$, in which case $\beta = \tanh z^\star$.

Likewise, we may wish to write the background velocity using a separate velocity scale u_0 and a nondimensional function γ:

$$U = u_0 \gamma,$$

an example being the linear function $U = u_0 z/h$, where $\gamma = z^\star$.

While these choices are easily made, one must then relate them back to their equivalents in the generalized scaling (6.23), for it is these that must be inserted into the solution algorithm (6.24).

6.4.1 Example #1: Shear Scaling

We have used this scaling frequently. The length and velocity scales are:

$$L = h \; ; \quad V = u_0,$$

and are intended to characterize the vertical variability of the background velocity profile $U(z)$. In this case we find that scaled viscosity and diffusivity defined in (6.23) have recognizable forms:

$$\nu^\star = \frac{\nu}{LV} = \frac{\nu}{hu_0} = \frac{1}{Re} \; ; \quad \kappa^\star = \frac{\kappa}{hu_0} = \frac{\nu}{hu_0}\frac{\kappa}{\nu} = \frac{1}{Re\,Pr}$$

Scaling the Buoyancy

Now suppose we choose the alternative form $B = b_0\beta$ for the background buoyancy profile, where b_0 is some buoyancy scale that suits the problem and β is a nondimensional function of $z^\star$. What should we then insert into the buoyancy "slot" in the solution algorithm?

$$B^\star = B\frac{L}{V^2} = b_0\beta\frac{h}{u_0^2} = \frac{b_0 h}{u_0^2}\beta(z^\star) = Ri_b\,\beta(z^\star).$$

The scaled buoyancy gradient is then

$$B^\star_{z^\star} = Ri_b\,\beta_{z^\star}.$$

For example, let $B = b_0\tanh(z/h)$, so that $\beta = \tanh z^\star$. Then the input to the solution procedure would be

$$B^\star_{z^\star} = Ri_b\,\beta_{z^\star} = Ri_b\,\text{sech}^2 z^\star.$$

With the above choices, the format for the solution algorithm is

$$[\sigma^\star, \hat{w}^\star, \hat{b}^\star] = \mathcal{F}(z^\star, U^\star, Ri_b\,\beta_{z^\star}, \frac{1}{Re}, \frac{1}{Re\,Pr}; \; k^\star, \ell^\star). \qquad (6.25)$$

6.4.2 Example #2: Diffusion Scaling

The shear scaling defined above ($L = h$; $V = u_0$) can be used in any situation as long as the background current is nonzero, i.e., $u_0 \neq 0$. If we need to allow for the possibility that $u_0 = 0$, we may do so by adopting the diffusive scaling. For example, we might wonder what happens to Benard convection when a uniform shear is imposed (Figure 6.1), retaining the option to set the background shear to zero as a special case. We therefore choose the length scale to be the domain height H as in the original Benard problem (section 2.4), and the diffusive velocity scale $V = \kappa/H$.

Using these scales, the nondimensional viscosity and diffusivity defined in (6.23) take very simple forms:

$$\nu^\star = \frac{\nu}{VH} = \frac{\nu}{\kappa} = Pr, \qquad (6.26)$$

$$\kappa^\star = \frac{\kappa}{VH} = 1. \qquad (6.27)$$
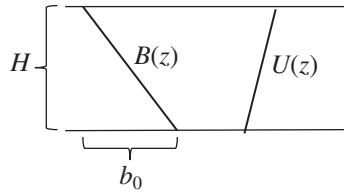
Figure 6.1 Definitions for the sheared Benard problem.

Scaling the Buoyancy

Suppose we choose the scaling $B = b_0 \beta$ for the buoyancy profile (where b_0 is some buoyancy scale that suits the problem, e.g., Figure 6.1, and β is a nondimensional function of $z^\star$ as described previously). In the solution algorithm (6.24), the buoyancy gradient input is determined as follows:

$$B^\star = B \frac{H}{V^2} = b_0 \beta \frac{H}{\kappa^2/H^2} = \frac{b_0 H^3}{\kappa^2} \beta = \frac{b_0 H^3}{\kappa \nu} \frac{\nu}{\kappa} \beta = Ra\, Pr\beta \Rightarrow B^\star_{z^\star} = Ra\, Pr\, \beta_{z^\star}.$$

For the linear profile $B = -b_0 z/H$ (Figure 6.1), $\beta = -z^\star$. Then the input to the solution algorithm would be $B^\star_{z^\star} = Ra\, Pr\, \beta_{z^\star} = -Ra\, Pr$.

Scaling the Velocity

Now suppose we want to impose a background velocity

$$U = u_0 \gamma,$$

where u_0 is a suitable velocity scale and γ is a nondimensional function. The appropriate input to the solution algorithm would be

$$U^\star = \frac{U}{V} = \frac{u_0 \gamma}{\kappa/H} = \frac{u_0 H}{\kappa} \gamma = \frac{u_0 H}{\nu} \frac{\nu}{\kappa} \gamma = Re\, Pr\gamma.$$

For example, we may assume a linear background shear as in Figure 6.1: $U = u_0 z/H$. In this case the velocity slot in the solution procedure would be filled by $U^\star = Re\, Pr z^\star$. The special case of zero background flow corresponds to the limit $Re \to 0$.

In summary, using the diffusive scaling with alternative forms for both buoyancy and velocity, the solution algorithm has the form:

$$[\sigma^\star, \hat{w}^\star, \hat{b}^\star] = \mathcal{F}(z^\star, Re\, Pr\, \gamma, -Ra\, Pr\, \beta_{z^\star}, Pr, 1; k^\star, \ell^\star). \tag{6.28}$$

Keep in mind that the solution algorithm $\mathcal{F}$ has not changed since it was first defined in (6.16). The procedures outlined in this and the previous section will enable you to use it to solve a wide range of theoretical and observational problems.

6.5 Application: Instabilities of a Stably Stratified Shear Layer

Back in section 4.6, we studied Kelvin-Helmholtz and Holmboe instabilities using a highly simplified analytical model of an inviscid fluid. Here, we study the corresponding phenomena in a more realistic context, including the effects of viscosity and diffusion, using smoothly varying profiles, and solving the equations via the numerical techniques developed in this chapter.

Consider a stratified shear layer in which the velocity and the buoyancy may change over different length scales:

$$U^\star = \tanh z^\star ; \quad \beta = \tanh Rz^\star, \qquad (6.29)$$

where shear scaling (section 6.4.1) is used and the constant parameter R is the ratio of shear layer thickness (Figure 6.2a) to stratified layer thickness (Figure 6.2b). While the case $R = 1$ is the most common, flows with $R > 1$ are frequently found in seawater, where momentum diffuses faster than buoyancy (Table 1.1). In this section we'll discuss cases with $R = 1$ and $R = 3$.

In the inviscid limit, the Miles-Howard theorem (section 4.7) requires that Ri be less than 1/4 somewhere in the flow. Here we will assume that Re is large so that the frozen flow hypothesis is valid and the Miles-Howard theorem is approximately valid.[3] When $R = 1$, the Richardson number is a minimum at the center of the shear layer (Figure 6.2c, blue). The Miles-Howard criterion therefore requires that $Ri_b < 1/4$. An exact expression is available for the stability boundary on the $k^\star - Ri_b$ plane (section 4.4):
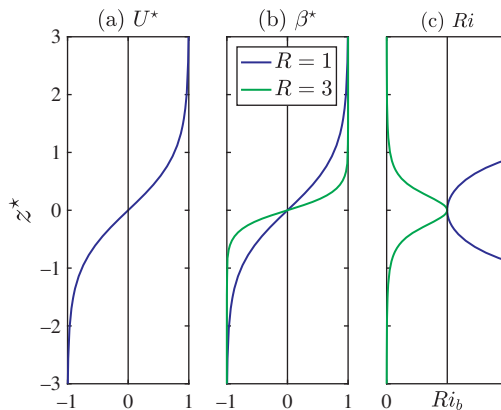

Figure 6.2 (a) Scaled velocity and (b) buoyancy profiles for the Holmboe model (6.29) with $R = 1, 3$. (c) Ri profile for the case $Ri_b = 0.1$, or $Ri_0 = 0.3$. Asterisks indicate shear scaling (section 6.4.1).

---

[3] If $Re \gg 1$, the only effect is a change in the critical Richardson number proportional to $1/Re$ (Thorpe et al., 2013). In the present cases the difference is negligible.

$$Ri_b = k^\star(1 - k^\star). \tag{6.30}$$

The critical state for instability is $k^\star = 1/2$, $Ri_b = 1/4$.

When $R \neq 1$, the value of Ri at the center of the shear layer is different from Ri_b. We call that central value Ri_0; it is equal to $Ri_b R$. In the case $R = 3$, Ri decreases from Ri_0 at the center of the shear layer to zero at infinity (Figure 6.2c, green), so the Miles-Howard criterion is satisfied regardless of how large Ri_0 is. As you might guess, this distinction has a profound effect on the nature of the instability.

6.5.1 Kelvin-Helmholtz Instability

Of all the instabilities of a stratified, parallel shear flow, the Kelvin-Helmholtz instability is probably the most commonly observed in nature. A stationary instability, it grows in place to form a train of co-rotating vortices that visually resemble surface waves breaking on a beach (e.g., Figure 6.4). These finite-amplitude manifestations of the instability are called Kelvin-Helmholtz billows. The underlying vortical structure is revealed more clearly in an echosounder image (Figure 6.5). For other examples, see Figures 4.4, 4.5, and 12.1 and Smyth and Moum (2012), or do a web search on "Kelvin-Helmholtz clouds."

Figure 6.3 shows the growth rate $\sigma^\star(k^\star, Ri_b)$ for the case $R = 1$, computed numerically using the methods of section 6.2. Viscosity is weak ($Re = 200$), and impermeable, frictionless boundaries are placed at $z^\star = \pm 5$. In the homogeneous limit $Ri_b = 0$, this is just the hyperbolic tangent shear layer discussed in section 3.9.1. The growth rate reaches a maximum value $\sigma^\star = 0.19$ at $k^\star = 0.44$, consistent with the previous results.

As Ri_b is increased, the growth rate decreases, indicating the damping effect of the stable buoyancy stratification. The wavenumber of the fastest-growing mode increases slightly. The stability boundary is similar to the inviscid result (6.30), but several differences are evident. For $k^\star > 0.5$, the stability boundary is slightly lower. This shows that, in the presence of viscosity, lower Ri_b is required for growth. Modes with smaller wavenumbers, $k^\star < 0.5$, are less affected by viscosity, but they are more susceptible to the influence of boundaries. The boundaries tend to enhance growth in this regime.

6.5.2 Holmboe Instability

We turn now to the case $R = 3$, i.e., where the stratification covers only the inner 1/3 of the shear layer (Figure 6.2, green curves). In the homogeneous limit $Ri_0 \rightarrow 0$, the value of R is irrelevant and we once again have a hyperbolic
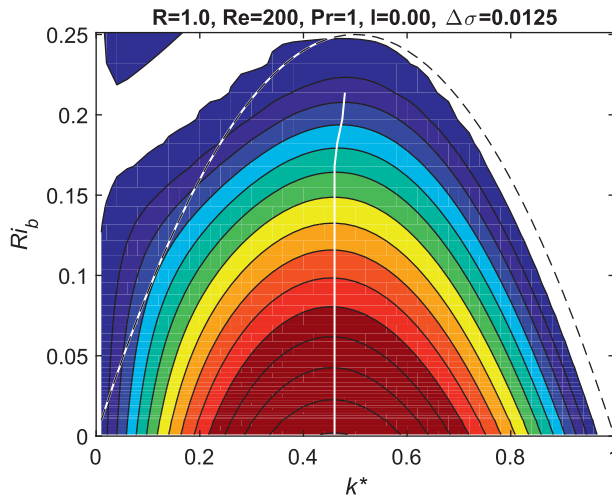
Figure 6.3 Growth rate versus scaled wavenumber and central/bulk Richardson number for the hyperbolic tangent profiles (6.29) with $R = 1$; $Re = 200$; $Pr = 1$. Only two-dimensional modes ($\ell^\star = 0$) are shown. The contour interval is 0.0125, starting at zero. Instability is stationary. The solid white curve indicates the fastest-growing mode at each Ri_b. Dashed curve shows the exact stability boundary for the limit of zero viscosity and infinite domain height. Frictionless, constant-buoyancy boundaries were placed at $z^\star = \pm 10$; grid increment was $\Delta^\star = 0.1$.

Figure 6.4 Kelvin-Helmholtz billow clouds, courtesy Brooks Martner, NOAA.

tangent shear layer with growth rate maximized at $k^\star = 0.44$ (Figure 6.6). If the stratification is sufficiently weak, the shear drives Kelvin-Helmholtz instability not much different from that found in the $R = 1$ case, although the wavenumber decreases markedly with increasing Ri_0. When the stratification is strong, Kelvin-Helmholtz instability is supplanted by Holmboe instability. The boundary
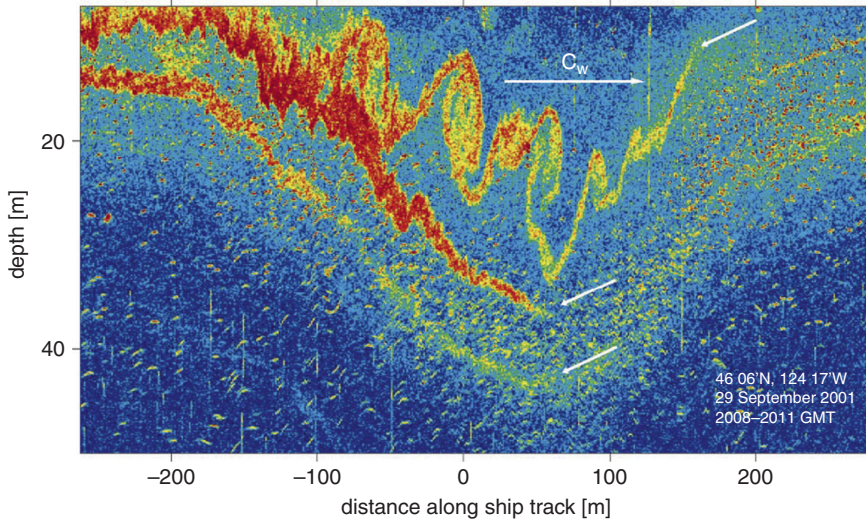
Figure 6.5 Echosounder image of a nonlinear internal wave propagating over the continental shelf toward the Oregon coast. C_w indicates the direction of wave propagation. Upper currents are in the direction of propagation, setting up a shear within the wave. Note the difference in horizontal and vertical scales; at any x, the flow is approximately a parallel shear flow. Short arrows identify three layers where disturbances grow as the wave passes. The uppermost layer forms a clearly resolved train of Kelvin-Helmholtz billows. The lower two layers are too thin for the growing disturbances to be well resolved. Reproduced from Moum et al. (2003).

between the two is approximately (but not exactly) $Ri_0 = 1/4$, and varies strongly with R.

Note the similarity between the stability diagrams in Figures 6.6 and 4.11(b). Both exhibit transitions between Kelvin-Helmholtz and Holmboe instabilities for increasing Richardson numbers. This suggests that the essential mechanisms of the instabilities are captured in the simple piecewise profiles. In our previous discussion of the Holmboe instability (section 4.6.3) we found that it is driven by a resonance of vorticity waves and gravity waves. The threshold stratification corresponds to Ri_0 somewhat greater than 1/4 (Figure 6.6). Above this threshold, the growth rate increases with increasing Ri_0 until a maximum is reached (at $Ri \approx 1$ for the case shown in Figure 6.6). Between these values, it is possible that the fastest growing mode is oblique (see section 6.3).

In the example shown in Figure 6.7, the fastest growing Holmboe instability is in fact oblique, with wave vector directed about 45 degrees from the streamwise direction. By symmetry, there is an accompanying mode with the opposite angle of obliquity. The result, viewed from above or below, is a diamond pattern of standing oscillations growing exponentially in time.
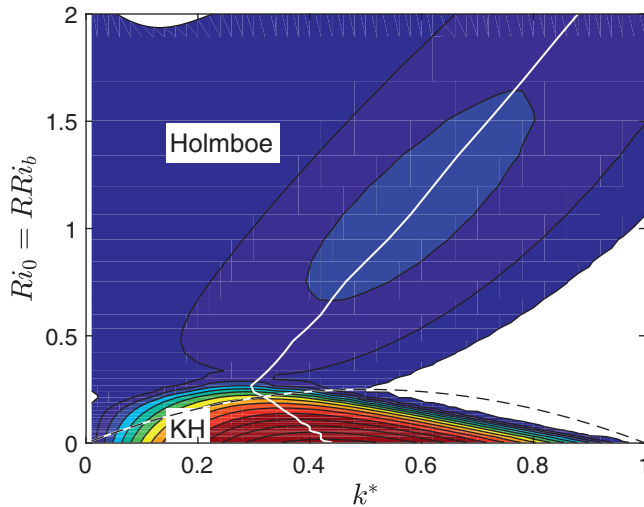
Figure 6.6 Growth rate versus scaled wavenumber and central Richardson number for the Holmboe profiles (6.29) with $R = 3$; $Re = 200$; $Pr = 9$. The contour interval is 0.0125, starting at zero. Instability is stationary in the lower lobe (Kelvin-Helmholtz instability); oscillatory in the higher (Holmboe instability). The dashed curve shows the inviscid stability boundary for $R = 1$, for comparison. Frictionless, constant-buoyancy boundaries were placed at $z^\star = \pm 10$; grid increment was $\Delta^\star = 0.1$. The solid white curve denotes the fastest-growing mode. The black dashed curve is the stability boundary for the case $R = 1$.
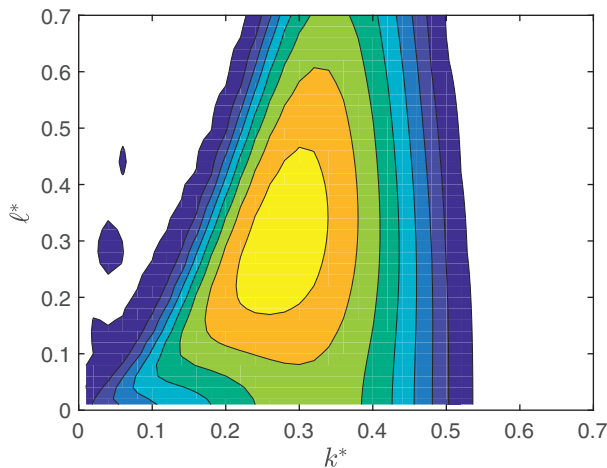

Figure 6.7 Holmboe instability growth rate versus scaled wavenumbers $k^\star$ and $\ell^\star$ for $Re = 200$ and $Ri_0 = 0.3$. The contour interval is 0.002, starting at zero. The fastest-growing mode is oblique.

6.6 Application: Analysis of Observational Data

Figure 6.8 shows profiles of currents and stratification observed just west of the Straits of Gibraltar (Nash et al., 2012). Current profiles (Figure 6.8a) include the zonal and meridional components, and extend to 450 m depth (just above the bottom). Both components show a distinct bottom current, directed southwest into the Atlantic. This is the Mediterranean Outflow, a gravity current driven by the high salinity (and thus high density) of the Mediterranean water. Above the outflow is a weak, nearly zonal return flow of fresher Atlantic water.

The buoyancy profile (Figure 6.8b) shows that the water column is stratified in the upper 150 m and near the bottom, but is much more homogeneous in the upper flank of the outflow and for about 100 m above that, indicating that the flow is, or has recently been, strongly turbulent.
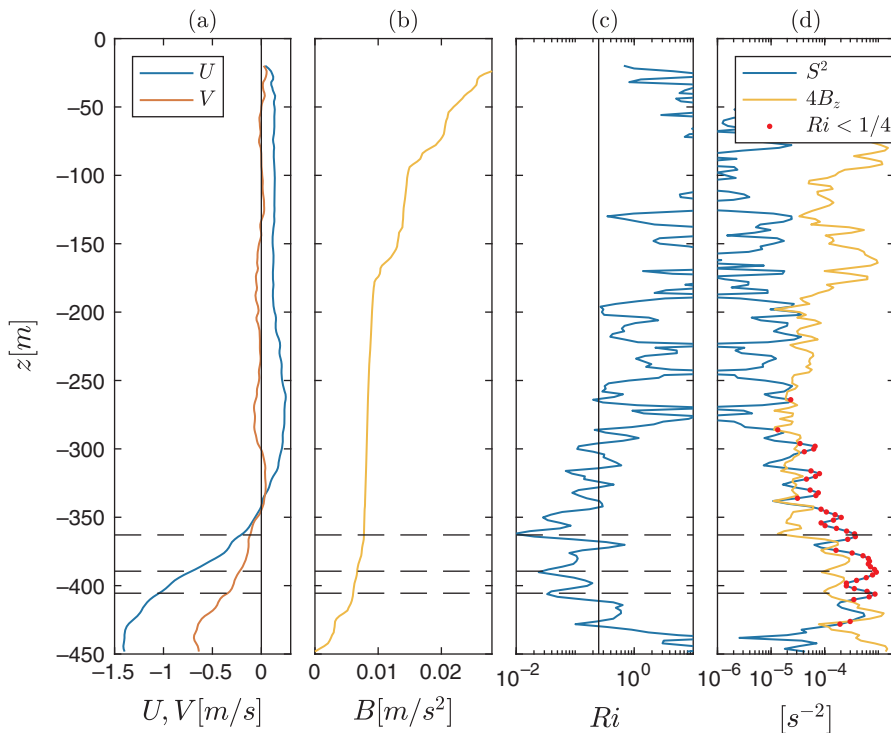

Figure 6.8 Profiles from the Mediterranean Outflow (Nash et al., 2012). (a) Zonal (blue) and meridional (red) current velocity. (b) buoyancy relative to the bottom. (c) Gradient Richardson number. (d) Squared shear magnitude (blue), and 4 times squared buoyancy frequency (yellow). Red dots show depths where $Ri < 1/4$. Horizontal lines show critical levels for the three fastest-growing instabilities. (Data courtesy of Jon Nash, Oregon State University.)

The gradient Richardson number Ri (Figure 6.8c) is high in the upper 300 m and near the bottom, but is low in the Outflow. At several points, $Ri < 1/4$, suggesting the possibility of instability. This possibility is further emphasized by the squared shear (Figure 6.8d, blue), which is high in regions of low Ri (red dots in Figure 6.8d). Shear maxima often coincide with minima of the buoyancy gradient (yellow). Based on these profiles, one could hypothesize that shear instability is common on the upper flank of the Outflow. That hypothesis can be tested via numerical solution of the perturbation equations.

To prepare for this analysis, the profiles were interpolated onto a regular vertical grid with spacing $\Delta = 2$ m and lowpass filtered with cutoff of 12 m. The squared shear, averaged over the water column, is greatest in the direction $\phi = 25°$ from current, roughly the direction of the outflow. Stability analysis was carried out using the current projected onto this direction: $\tilde{U} = U \cos\phi + V \sin\phi$, equivalent to looking for instabilities with wave vectors pointed in this direction (cf. section 4.12).[4]

A grid of wavelengths $\lambda = 2\pi/\tilde{k}$ was chosen, ranging from 32 m to 10 km. The reason for this choice is the rule of thumb for a shear layer instability: the wavelength is about 7 times the thickness of the shear layer (e.g., Table 3.1 or summary of Chapter 4). After applying the 12 m lowpass filter, the thinnest shear layer resolvable has thickness $h \sim 6$ m, so we can guess that it would produce an instability with $\lambda \sim 40$ m. The longest wavelength, 10 km, is intended to approximate a hydrostatic gravity wave whose vertical structure covers the whole water column. That wavelength was arrived at by trial and error. Modes at the short end of this range are poorly resolved and are considered highly approximate. Resolution is discussed in greater detail in Chapter 13.

To represent smoothing by ambient, small-scale turbulence, viscosity and diffusivity were set to $\nu = \kappa = 1 \times 10^{-4} \text{m}^2/\text{s}$. Frictionless, insulating boundary conditions were imposed at the surface and at the bottom. For each λ, the three fastest-growing eigenvalues were saved.

When several modes are retained, the dependence of the resulting growth rates on the wavelength can be difficult to make sense of, especially if the obliquity angle ϕ is also varied. The solution is to examine the depth of the critical level for each mode, as these tend to align themselves into a much more coherent pattern. The critical level depths are approximately independent of wavelength, at least over the range of wavelengths where the growth rate is large. Three depths are shown by horizontal lines on Figure 6.8. Upon close inspection, one can see that each depth coincides closely with a local maximum of the shear magnitude (cf. Shear Production Theorem, section 3.11.2). Therefore, each of the peaks in the

---

[4] This is a bit of corner-cutting. Ideally, one would scan over a range of directions to account for the veering of the flow with depth.
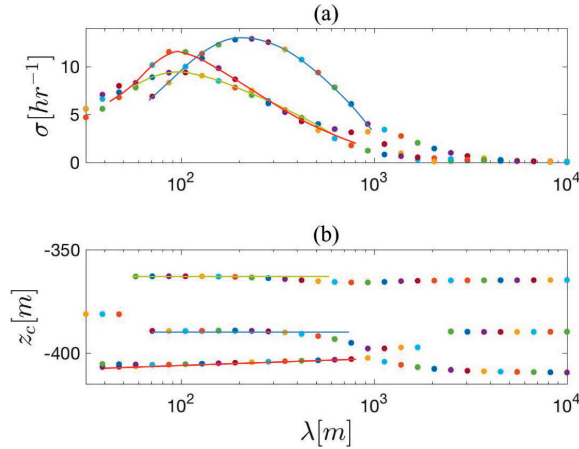
Figure 6.9 (a) Growth rates, and (b) critical level depths, versus wavelength for the three fastest-growing modes. Points are color coded for manual matching of σ's with z_c's.

growth rate shown in Figure 6.9a represents instability growing on a particular shear layer. We refer to such a grouping as a mode family and are most interested in the fastest-growing mode of each family.

For this simple case the growth rates and critical levels were matched by hand using the color-coding of the data points, and thereby organized into mode families as sketched on Figure 6.9. For more extensive datasets, one can automate the process by constructing a histogram of z_c. Mode families are then identified by peaks in the histogram.

Each of the three mode families seen on Figure 6.9a has its own fastest-growing mode and its own critical level. Of these, the most unstable (identified by the blue curve) has z_c at about 390 m depth (middle dashed line on Figure 6.8). Its growth rate is 14 hr^{-1}, so its amplitude grows by a factor $e = 2.718$ in about four minutes. The growth rate peaks at a wavelength a little over 200 m. According to our factor-of-7 rule this suggests a shear layer thickness around 30 m. Close inspection of Figure 6.8b bears this out: a shear maximum is visible at about 390 m depth, and 30 m would be a reasonable estimate of its thickness.

The second fastest mode (highlighted in red on Figure 6.9a) is considerably shorter, with wavelength 100 m, and has critical level at 410 m. The third mode (yellow) is focused at 360 m depth. It also has wavelength 100 m, but a much slower growth rate. Close inspection of Figure 6.8a shows corresponding shear maxima at 410 and 360 m, and in each case the peak shear is roughly consistent with the growth rate (reduced at 410 m, reduced further at 360 m). Both shear maxima are thinner than the one at 390 m, explaining the shorter wavelengths.
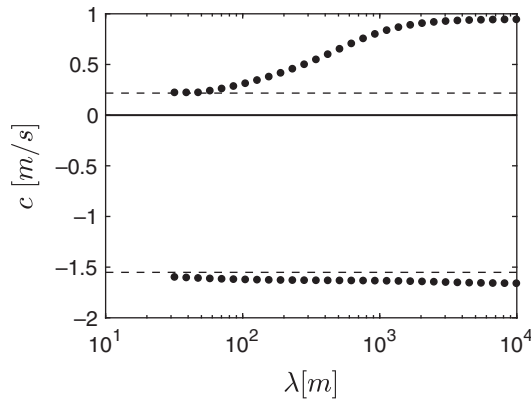
Figure 6.10 Phase velocities of the fastest upstream and downstream neutrally propagating internal waves as a function of wavelength.

None of these modes is associated with the upper flank as a whole[5]. That shear layer is about 100 m thick and would therefore support instabilities of about 700 m wavelength. In reality, these are damped by the close proximity of the bottom. (To learn about boundary effects, try exercise 12.) Instead, instabilities grow on smaller, more intense shear layers that develop more or less at random within the larger shear flow.

One possibility is that each of these instabilities creates turbulence, which then mixes out the shear layer that spawned it, returning Ri to values above 1/4 until gravity accelerates the flow once again. This process, called cyclic instability, is discussed further in section 12.3. Another possibility is that the "shear layer" is actually a disruption of the measurements by an inquisitive sea creature. (Despite concerns about the impending extinction of ocean life, such encounters are frustratingly common, e.g., Pujiana et al., 2015).

Besides instabilities, one is often interested in neutrally stable wave modes supported by observed profiles. These are obtained by simply rearranging the computed eigenmodes to pick out those for which σ is nearly imaginary, e.g., $|\sigma_r/\sigma_i| < 10^{-3}$. We then compute the phase speed $c = -\iota\sigma/k$. Because the boundaries are fixed, the extremely fast surface and barotropic wave modes are excluded; what this calculation gives us are the baroclinic modes (first, second, etc.) as modified by whatever background current may be present.

For the Mediterranean Outflow profiles, the wave modes with fastest propagation upstream and downstream are shown in Figure 6.10. As is typical of internal gravity waves, the phase speed increases with increasing wavelength, asymptoting to a limiting value when the wavelength is several kilometers or more. Note that

[5] Meaning the main shear layer extending between about 330 m and 430 m depth.

both modes have phase speeds outside the range of the background velocity, i.e., they do not have critical levels. This suggests that the Mediterranean outflow is hydraulically subcritical, i.e., information can propagate both upstream and downstream, hence we would not expect to find an internal hydraulic jump, at least at this time and location.

6.7 Summary

Combining results from Chapters 2 through 5, we have developed a versatile set of techniques for the analysis of instabilities and waves in stratified shear flows. Viscosity and diffusion may originate with molecular effects or with turbulence, and may be included either for physical realism or as a numerical strategy to reduce resolution requirements. Besides idealized models like the Kelvin-Helmholtz and Holmboe shear instabilities, we have seen how the techniques may be applied to observational data.

6.8 Further Reading

See Smyth and Moum (2012) for an overview of Kelvin-Helmholtz instability in the ocean. More information on Holmboe instability is in Carpenter et al. (2010). Lab experiments confirming the linear theory of Kelvin-Helmholtz and Holmboe instabilities may be found in Thorpe (1973) and Tedford et al. (2009b). Further examples of normal mode analysis applied to observational data are Putrevu and Svendsen (1992), Einaudi and Finnigan (1993), Sun et al. (1998), Tedford et al. (2009a), Moum et al. (2011), Smyth et al. (2011), and Smyth et al. (2013).